Kinetics of the Methanol Reaction with OH at Interstellar, Atmospheric, and Combustion Temperatures

Lu Gem Gao,[1] Jingjing Zheng,[2] Antonio Fernández-Ramos,[4] Donald G. Truhlar,[3,*] and Xuefei Xu[1,*]

[1]*Center for Combustion Energy and Department of Energy and Power Engineering, Tsinghua University, Beijing 100084, China*
[2]*Gaussian, Inc., 340 Quinnipiac St., Bldg. 40, Wallingford, CT 06492 USA*
[3]*Department of Chemistry, Chemical Theory Center, and Minnesota Supercomputing Institute, University of Minnesota, Minneapolis, Minnesota 55455-0431, USA*
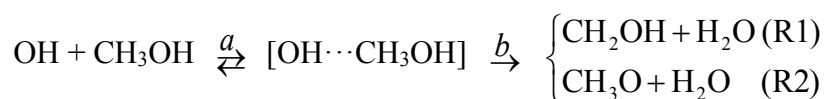[4]*Centro Singular de Investigación en Química Biolóxica e Materiais Moleculares (CIQUS), c/Jenaro de la Fuente s/n, Campus Vida, Universidad de Santiago de Compostela, 15782-Santiago de Compostela, Spain*

ABSTRACT: The OH radical is the most important radical in combustion and in the atmosphere, and methanol is a fuel and antifreeze additive, model biofuel, and trace atmospheric constituent. These reagents are also present in interstellar space. Here we calculate the rate constants, branching ratios, and kinetic isotope effects (KIEs) of the hydrogen abstraction reaction of methanol by OH radical in a broad temperature range of 30–2000 K, covering interstellar space, the atmosphere, and combustion by using the competitive canonical unified statistical (CCUS) model in both the low-pressure and high-pressure limits and, for comparison, the pre-equilibrium model. Coupled cluster CCSD(T)-F12a theory and multireference CASPT2 theory were used to carry out benchmark calculations of the stationary points on the potential energy surface to select the most appropriate density functional method for direct dynamics calculations of rate constants. We find a significant effect of the anharmonicity of high-frequency modes of transition states on the low-temperature rate constant, and we show how tunneling leads to an unusual negative temperature dependence of the rate constants in the range 200 K > T > 100 K. The calculations also demonstrate the importance of the extent of stabilization of the pre-reactive complex. The capture rate for the formation of the complex is the dominant dynamical bottleneck for T < 100 K, and it leads to weak temperature dependence of the rate below 100 K in the high-pressure-limit of the CCUS model. We also report the pressure dependence of branching ratios (which are hard to measure so theory is essential) and the KIEs, and we report an unusual nonmonotonic variation of the KIE in the high-pressure limit at low temperatures.

1. INTRODUCTION

The use of clean-burning oxygenated fuels, for example, alcohol biofuels, for ground transportation provides a way to mitigate the increasingly serious problem of air pollution. As the simplest alcohol, methanol is an inexpensive fuel additive for internal combustion engines. In addition, methanol is usually present in small amounts in the atmospheric environment, where it plays a role in atmospheric chemistry. There is a large amount of kinetics research on elementary reactions involving methanol;[1] and the reaction of methanol with OH radical has been of special interest because OH radical is one of the main oxidizing reactive species in both combustion and the atmosphere.[2,3,4,5,6,7,8,9,10] Methanol is also one of the most abundant organic molecules in interstellar space, and the reaction of methanol with OH to produce methoxy also occurs in the ultracold environment of interstellar space,[11] where its observation is one of the more stunning examples of quantum mechanical tunneling.

The reaction has two products; the OH radical can abstract an H atom from either the methyl (reaction R1) or the hydroxyl (reaction R2) group of methanol. We will consider the following two-step model of the reaction:

$$OH + CH_3OH \; \overset{a}{\rightleftharpoons} \; [OH \cdots CH_3OH] \; \overset{b}{\rightarrow} \; \begin{cases} CH_2OH + H_2O \; (R1) \\ CH_3O + H_2O \quad (R2) \end{cases}$$

Step a is the complexation reaction, which is the same for R1 and R2. The reverse of the complexation reaction is called step -a; the rate constants for these steps are called k_a and k_{-a}, and the equilibrium constant is

$$K_a = k_a/k_{-a} \tag{1}$$

The rate constant for step b is called $k_{b,1}$ for R1 and $k_{b,2}$ for R2.

In the pre-equilibrium model (PEM), the complex is fully equilibrated and thermalized, and we may write the overall rate constants as

$$k_{R1}^{PEM} = K_a \, k_{b,1} \tag{2}$$

and

$$k_{R2}^{PEM} = K_a \, k_{b,2} \tag{3}$$

This is the high-pressure limit of the two-step model in the hypothetical case where reaction is slow compared to the collisional equilibration of the complex so that the complex is fully equilibrated. This limit, although interesting as a model, is not expected to be achieved in practice when the second step is fast. Therefore, we will consider two other models, in

particular the low-pressure and high-pressure limits of the competitive canonical unified statistical (CCUS) model.[12]

In the low-pressure limit (LPL), the complex is never formed and the mechanism involves only a single step:

$$OH + CH_3OH \xrightarrow{c} \begin{cases} CH_2OH + H_2O \; (R1) \\ CH_3O + H_2O \quad (R2) \end{cases}$$
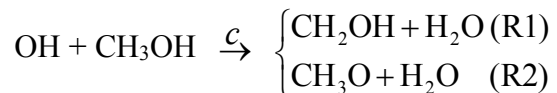
where

$$k_{R1}^{LPL} = k_{c,1} \tag{4}$$

and

$$k_{R2}^{LPL} = k_{c,2} \tag{5}$$

In practice, the low-pressure limit of the CCUS can be quite different from the pre-equilibrium model because the pre-equilibrium model involves the possibility of tunneling to the product from low-energy states of the complex produced by energy-transfer collisions with a high-pressure bath gas, whereas the single-step model involves no states of the system with energy below the ground-state energy of the reactants (note that production of the complex and the product are both exoergic, but in a single collision, the total energy is constant and cannot be lower than the lowest energy state of the reactants, which is reactants in their zero-point level and zero translational energy). At intermediate pressures, the complex is present but unequilibrated, which makes the situation more complicated, and the rate constant is in the so-called falloff region, where it is somewhere between these two limits. We will see that at low temperature even the high-pressure limit of the CCUS is quite different from the PEM; in this case, the difference is because the first dynamical bottleneck becomes rate limiting at low temperature.

Early study of the $CH_3OH + OH$ kinetics only involved temperatures above 210 K because both of the possible reactions R1 and R2 have a barrier to form products, and reactions with a barrier are considered less important in low-temperature chemistry. Recently though, Shannon et al.,[11] by using a pulsed Laval-nozzle apparatus with flash photolysis, measured a surprisingly large rate coefficient at 82 and 63 K, an unexpectedly large negative dependence of the rate constant on temperature below 200 K, and an unexpectedly higher branching fraction of R2 at lower temperatures, despite this reaction having a larger barrier than R1. Their discovery revealed the potential importance of the $CH_3OH + OH$ reaction in cold interstellar space and motivated further investigations at the ultra-low temperatures of interest for understanding interstellar chemistry.[13,14,15,16] These follow-up studies all

confirmed the observations of Shannon et al., although there are important discrepancies about the interpretation of those observations.[16] By interpreting their experiments with a master equation incorporating quantum-mechanical tunneling, Shannon et al. attributed the mechanism behind the unexpected negative temperature dependence of the rate coefficient for this reaction to tunneling through the barrier via a long-lived hydrogen-bonded pre-reactive complex at low temperatures.

Previously a negative temperature dependence of the total reaction rate at low temperatures was also observed in other alcohol reactions with OH, for example, isobutanol + OH[17] and 2-butanol + OH,[18] for both of which the negative temperature dependence of the rate constant was observed up to higher temperatures, about 400 K, than for methanol, and it was shown that the anharmonicity of high-frequency vibrational modes in the transition-state (TS) structures is important for predicting the quantitative rate constants at low temperatures.

Questions arise. Does the anharmonicity of the TS structure also play an important role in the methanol + OH reaction, and if yes, what is the combined effect of tunneling and anharmonicity on the rate constant at ultracold temperatures? Is a necessary condition for negative temperature dependence that the system tunnels from pre-reactive complex states at lower energy than the reactant state, as previous works[11,16] suggested? What is the temperature dependence of the product branching fractions, which are not observed in typical rate constant measurements where only the sums of the reaction rates for R1 and R2 are measured? To answer these questions, and also to provide a unified treatment of this reaction that spans the broad temperature range encompassing the interstellar, atmospheric, and combustion regimes, the present article employs the CCUS model, in which the individual dynamical bottlenecks are treated by multistructural variational transition-state theory[19] with multistructural torsional anharmonicity based on a coupled torsional potential,[20,21,22,23] and with the small-curvature tunneling approximation[24] (MS-CVT/SCT). The CCUS model is a straightforward extension of the canonical unified statistical model.[25,26,27,28] We use the low-pressure and high-pressure limits of the CCUS to calculate the rate constants of the two methanol + OH reactions (R1 and R2) over the temperature range 30 to 2000 K.

In the present calculations, specific-reaction-parameter (SRP) scaling factors optimized for individual complexes and transition states,[17] have been used for vibrational frequencies of transition states and the complexes to take into account more accurately the anharmonicity of zero-point energies (ZPEs).

The work will be presented as follows: the pre-dynamics computational details and methods are given in sections 2 and 3; and the dynamics methods and low-pressure and high-

pressure limits of the CCUS are described in section 4. In section 5, the calculated rate constants of the two reactions are compared with representative kinetic data from the literature, and the product branching fractions and kinetic isotope effects are presented. A summary is given in section 6.

2. ENERGIES AND STRUCTURES

2.1 Selection of Model Chemistry for Calculations of Potential Energy Surfaces

Our first task was to choose the most appropriate model chemistry for potential energy surface (PES) calculations of each reaction. To do this, we tested the performance of a variety of Kohn-Sham (KS) model chemistries by calculations of the classical reaction energies and barrier heights of the two reactions by comparing their results to the best estimates we could obtain.

The tested KS model chemistries are selected combinations of the M08-HX[29], M08-SO[29], MN15[30], M06-2X[31], MN15-L[32], ωB97X-D[33], B3LYP[34], MPW1K[35], and M05-2X[31] exchange-correlation functionals with the aug-cc-pVTZ[36], jun-cc-pVTZ[37], jul-cc-pVTZ[37], MG3S[38], and 6-31+G(d,p)[39,40] basis sets. (Note that for the system considered here, MG3S is the same as 6-311+G(2df,2p).) Using these methods, the geometries of the reactants, pre-reaction complex, transition structures, and products were optimized, and were confirmed to be the desired stationary points by frequency calculations. Then the classical reaction energies and forward and reverse barrier heights were calculated.

2.2 Best Estimates for Classical Reaction Energies and Barrier Heights

The classical reaction energy, ΔV, is defined as the difference between the equilibrium potential energies of the products and the reactants; the classical barrier height, $V^{\neq}$, is the potential energy difference between the transition structure (saddle point) and the reactants. An accurate ΔV may be inferred from experiments, but $V^{\neq}$ is not available from experiment. We therefore chose a highly accurate theoretical method to compute a benchmark for $V^{\neq}$. Based on our experience, the CCSD(T)[41] coupled cluster method with the F12a[42] method to include explicitly correlated basis functions can give a realistic estimate for a system that is well described by a single configuration state function, but when one or more species with inherently multiconfigurational character are involved in the reaction, a multireference method, for example, complete active space second-order perturbation theory (CASPT2), may be needed for accurate calculations. Therefore, we calculated the T_1 diagnostic[43] (which is an indication of multireference character) for all species to estimate their extent of multi-

reference character using the structures optimized by M08-HX/MG3S. The T_1 values are shown in Table 1, and they may be interpreted in light of the experience that a T_1 value larger than 0.02 for a closed-shell system or 0.045 for an open-shell system means that a multi-reference method might be needed.[44] Based on these criteria, the single-reference CCSD(T)-F12a method should be accurate enough for the calculations of the classical reaction energy of the two reactions R1 and R2 and the barrier height of the reaction R1, but the multi-reference CASPT2 method with an appropriate active space is needed for calculating the barrier height of reaction R2 because its transition state TS2 has a T_1 value of 0.055. We also calculated M diagnositics[48] and these too indicate that TS2 has the largest multireference nature; the calculated M values are given in the Supporting Information.

2.2.1 Benchmark for R1: CCSD(T)-F12a

A best estimate of ΔV can be obtained from experimental enthalpies of reaction $\Delta_r H_0^o$ at 0 K by subtracting the change in vibrational zero point energy (ZPE):

$$\Delta V = \Delta_r H_0^o - \Delta(\text{ZPE}) \tag{6}$$

where the quantities on the right-hand side can be obtained from the experimental enthalpies of formation $\Delta_f H_0^o$ at 0 K of the reagents[45] and from previous estimates[1e,46] of ZPEs:

$$\Delta_r H_0^o = \sum \Delta_f H_0^o\,(P) - \sum \Delta_f H_0^o\,(R) \tag{7}$$

$$\Delta(\text{ZPE}) = \sum \text{ZPE}\,(P) - \sum \text{ZPE}\,(R) \tag{8}$$

The data used in the present work are listed in Table 2, and these data yield our best estimate of ΔV as -21.81 ± 0.60 kcal/mol for reaction R1 and -12.42 ± 0.76 kcal/mol for reaction R2.

We know from previous work that M08-HX/MG3S gives accurate internuclear distances at transition states,[47] and so it is a good choice for obtaining geometries for benchmark calculations. Tables 3 and 4 show the classical reaction energies calculated by CCSD(T)-F12a/jun-cc-pVTZ//M08-HX/MG3S are -21.88 and -12.32 kcal/mol for R1 and R2 reactions, respectively; these values agree within the experimental error bars with the best estimates. In light of this agreement and the diagnostics of Table 1, we use CCSD(T)-F12a/jun-cc-pVTZ//M08-HX/MG3S results as benchmarks of the R1 reaction. The calculated forward and reverse barrier heights of R1 by this method are listed in Table 3, and they are 1.46 kcal/mol and 23.34 kcal/mol, respectively.

2.2.2 Benchmark for R2: CASPT2

Reaction R2 needs a multi-reference treatment, and for this case, we calculated the classical reaction energy and barrier heights using the CASPT2 method with the MG3S basis set based on the structures optimized by M08-HX/MG3S. We used the correlated participating orbitals (CPO) scheme.[48,49] In the CPO scheme, the orbitals chosen in active spaces are those including important static correlation effects on chemical reactions, for example, those participating strongly in bond breaking and bond forming, plus correlating orbitals. We examined several CPO active spaces; the detailed compositions of various active spaces are listed in Table S3 (the prefix S indicates that a table or figure is in Supporting Information), and the corresponding orbitals of TS2, reactants and products are shown in Figures S1-S3. Table S4 provides the calculated classical forward barrier heights and energies of reaction for R2 using CASPT2 method with different active spaces. The largest active space examined is of size (11,11), which includes the bond orbitals that break or form during the H transfer reaction and the electrons in these bonds plus four p orbitals geminal to bonds that are broken or formed and, for each of them, a correlating orbital (occupying approximately in the same space as the orbital it correlates); this is the moderate CPO (mod-CPO) scheme. This calculation yields a classical energy of reaction of -12.45 kcal/mol, in good agreement with the experimentally based best estimate, and we chose the CASPT2(11,11) results as the benchmark of the reaction R2. This yields a classical forward barrier height of 3.06 kcal/mol.

2.3 Conformers

The reactants (CH_3OH and OH), complex, and products (CH_2OH, CH_3O, and H_2O) of the methanol + OH reaction are all simple molecules with only one conformer, but the transition state of each reaction has more than one conformer due to the presence of the two torsional degrees of freedom associated with internal rotation around the two half-bonds involving the transferred hydrogen atom. After an exhaustive conformational search carried out with the *MSTor* program,[50] four distinguishable structures of transition state were found for each reaction. They consist of two pairs of mirror images for the transition state TS1 of R1 and one pair of mirror images and two C_s symmetric structures for the transition state TS2 of R2; these structures are given in Figure 2. Their relative energies are also listed in Figure 2, as obtained by the methods selected above.

2.4 Performance of Various KS Model Chemistries in Electronic Structure Calculations

The calculated classical energy of reaction (ΔV) and the forward ($V_f^{\ddagger}$) and reverse ($V_r^{\ddagger}$) barrier heights using selected KS model chemistries for both R1 and R2 reactions are listed in Tables 3 and 4, respectively, as well as the best estimates; results for a larger set of model chemistries (see references in section 2.1) are given in the Supporting Information. The barrier heights given in Tables 3 and 4 were obtained using the lowest-energy structure of each transition state. The performance of various KS model chemistries for the current systems was evaluated by calculating their individual mean unsigned percentage deviation (MUPD) of the forward and reverse barrier heights and energy of reaction. The calculated MUPDs for selected model chemistries are listed in Tables 3 and 4.

As shown in the two tables, among the tested KS model chemistries, the M08-HX/jun-cc-pVTZ model performs best for R1 with a MUPD of 3.7%, and the M08-SO/jun-cc-pVTZ model performs best for R2 with a MUDP of 8%; so we chose these two model chemistries for the potential energy surface calculations in the dynamics study for the two reactions. In particular, we used these model chemistries to generate direct dynamics calculations of the temperature-dependent reaction rate constants. The lowest-energy structures of all species obtained using these two methods are given in the Supporting Information.

3. ANHARMONICITY

We consider two kinds of anharmonicity, anharmonicity in the high-frequency modes that dominates the zero-point energy and anharmonicity in the low-frequency torsional modes that makes a significant contribution to the entropies and hence the free energies of reactants and transition states, especially at higher temperatures. These two kinds of anharmonicity are treated in sections 3.1 and 3.2, respectively.

3.1 Specific-Reaction-Parameter Scaling Factor

The anharmonicity of high-frequency vibrational modes affects the rate constants especially at low temperatures. Usually we scale calculated harmonic vibrational frequencies by an empirical scaling factor for a given model chemistry; using the harmonic oscillator formulas with scaled vibrational frequencies is called the quasiharmonic approximation. The generic scaling factors are parameterized to obtain accurate zero point energies (ZPEs) by correcting for anharmonicity and also for systematic errors in the electronic structure model chemistry.[51]

Recently, it has been found that although these parametrized scaling factors work well for stable molecules, they can be unsuitable for transition states of some reactions. For example, for the isobutanol + OH reactions, which are a similar reaction to the reactions studied here, the transition states were found to have stronger anharmonicity than the reactants, and a specific-reaction-parameter (SRP) scaling factor for each specific transition state had to be used to get the accurate rate constants.[17] Therefore, in the present study, we determined an SRP scaling factor λ^{ZPE} for each transition state of the two reactions in a similar way. We also determined and used an SRP scaling factor for calculating the zero point energy and partition functions of the weakly bound complex. For each of these species (TS or complex), λ^{ZPE} is factored as:[51]

$$\lambda^{ZPE} = \lambda^{Anh}\lambda^{H} \tag{9}$$

where λ^{Anh} denotes the correction for anharmonicity, and λ^{H} is the correction for the inexactness of the model chemistry.

The λ^{Anh} scaling factor is computed as the ratio of anharmonic ZPE to the ZPE computed in the harmonic approximation. Anharmonic ZPEs were calculated by hybrid,[52] degeneracy-corrected,[53] second-order[55,56,57] vibrational perturbation theory (HDCVPT2). We chose MPW1K/MG3S to calculate λ^{Anh} because the higher-order force constants converge better (with respect to grid size) with this kind of hybrid GGAs than with hybrid meta GGAs. The calculated anharmonic and harmonic ZPEs and the ratio of anharmonic ZPE to harmonic ZPE, i.e., λ^{Anh}, are given in Table 5. Table 5 also lists the λ^{H} for M08-HX/jun-cc-pVTZ and M08-SO/jun-cc-pVTZ model chemistries, determined by parametrization to reproduce the accurate harmonic frequencies in the F38/10 database,[51] and the corresponding specific-reaction-parametrized scaling factor λ^{ZPE} generated as the product of λ^{Anh} and λ^{H}.

Table 5 shows that the calculated SRP values of λ^{ZPE} for the lowest-energy structures of the transition states of R1 and R2 reactions are both 0.964; these values are much smaller than the standard λ^{ZPE} values 0.974 for M08-HX/jun-cc-pVTZ and 0.984 for M08-SO/jun-cc-pVTZ. The calculated SRP values of λ^{ZPE} for the pre-reactive complex are 0.969 and 0.980 for M08-HX/jun-cc-pVTZ and M08-SO/jun-cc-pVTZ levels, and these are relatively closer to the standard ones than are those for the transition states. The standard λ^{ZPE} has been confirmed to be reasonable for stable CH_3OH molecule in a previous study,[1e] and so the present results indicate greater anharmonicity of high-frequency modes of the transition states than the reactants for the present systems. (Previous work also found that the standard scaling factors were adequate for other stable molecules, notably isobutanol,[17] 2-butanol,[18]

and toluene.[58]) We use the individual SRP values of λ^{ZPE} for the calculations of zero-point energies, partition functions, and enthalpies. Table 6 gives the resulting enthalpies for complex formation and enthalpies of activation for the lowest-energy conformers of the transition state.

3.2 Multi-Structural Torsional Anharmonicity

For each species α (where α = R for methanol, C for complex, and TS1 or TS2 for the transition states), the multi-structural anharmonicity factor is calculated as

$$F^{\text{MS-T},\alpha} = \frac{Q_{\text{con-rovib}}^{\text{MS-T},\alpha}}{Q_{\text{rovib},1}^{\text{SS-HO},\alpha}} \tag{10}$$

where $Q_{\text{con-rovib}}^{\text{MS-T},\alpha}$ is the conformational-rotational-vibrational partition function of species α evaluated by multistructural torsional anharmonicity approximation with coupled torsional potential[22] (MS-T), and $Q_{\text{rovib},1}^{\text{SS-HO},\alpha}$ is the single-structure quasiharmonic oscillator approximation rotational-vibrational partition function of the global minimum structure for species α. In general $Q_{\text{con-rovib}}^{\text{MS-T},\alpha}$ contains the contributions from all the distinguishable conformers of the reactants and the transition states, and it includes both the effect of multiple structures and the effect of torsional potential anharmonicity; however, since methanol and the complex have only one distinguishable structure each, in those cases $Q_{\text{con-rovib}}^{\text{MS-T},\alpha}$ contains only torsional potential anharmonicity.

4. DYNAMICS METHODS

As introduced in section 1, there are two potential dynamical bottlenecks to each reaction: a free energy bottleneck (TSa) to the barrierless formation of the pre-reactive complex in the entrance region and a free energy bottleneck (TS1 for R1 or TS2 for R2) in the vicinity of potential energy barrier. Thus, both possible bottlenecks should be considered in calculating rate constants for a given reaction. A correct treatment of the pressure dependence at intermediate pressures would require a master equation[59,60,61,62,63,64,65] with accurate rate constants for the energy relaxation of the complex, and we will not pursue an accurate treatment of the energy transfer in the present work. Instead we evaluate one low-pressure model and two high-pressure models. In the high-pressure models, the two bottlenecks are passed in separate dynamical steps, but in the low-pressure limit they are passed in a single collision; to account for the occurrence of two bottlenecks separated by an

intermediate, we apply the CCUS model in the high-pressure limit, and we compare it to the pre-equilibrium model.

4.1 Low-Pressure-Limit CCUS Rate Constants

In the low-pressure limit, the generalized free energy of activation as a function of the reaction coordinate has a local maximum between reactants and the complex, a local minimum in the complex region, and a local maximum near the barrier for reaction R1 or R2. The generalized transition state theory rate constants calculated at these four positions (with the reactants being OH + CH$_3$OH for the calculation of all four rate constants) are labeled respectively as k_a, k^C, $k_{TS,1}$, and $k_{TS,2}$. Note that k_a is the same as defined in the introduction, and $k_{TS,j}$ is the rate constant computed for passage through TS1 or TS2 as if the first dynamical bottleneck were not present, and k^C is calculated in the same way as a transition-state rate constant but at the local minimum (it is the location of the complex) between the variational transition states rather than at a saddle point.[25,26] The rate constant expression for the CCUS model is

$$k_{c,j} = \left(\frac{k_{TS,1} + k_{TS,2}}{k_a} - \frac{k_{TS,1} + k_{TS,2}}{k^C} + 1 \right)^{-1} k_{TS,j}, \quad j = 1 \text{ or } 2 \tag{11}$$

We make the working assumption that $k^C \gg k_{TS,1} + k_{TS,2}$ because the complex has a lower energy than the transition states TS1 and TS2. Then this expression reduces to

$$k_{c,j} = \frac{k_a}{k_a + k_{TS,1} + k_{TS,2}} k_{TS,j}, \quad j = 1 \text{ or } 2 \tag{12}$$

where $k_{c,j}$ is the same as defined in the introduction. In the current study, we estimate the capture rate constant k_a using the hard-sphere collision rate constant formula:

$$k_a = \pi \left(\frac{d_{OH} + d_{methanol}}{2} \right)^2 \sqrt{\frac{8k_B T}{\pi \mu}} \tag{13}$$

where μ is the reduced mass of OH and methanol, and d_{OH} and $d_{methanol}$ are vdW diameters.

We use multi-structural canonical variational transition state theory (MS-CVT) with multidimensional tunneling to calculate $k_{TS,j}$. The choice of which multidimensional tunneling approximation to use has been discussed elsewhere.[66,67] We performed some test calculations with both small-curvature tunneling (SCT) and large-curvature tunneling (LCT) and obtained larger transmission coefficients with SCT; therefore, we use SCT for all the tunneling calculations in this paper.

In the low-pressure limit, the pre-reactive complex of CH_3OH and OH cannot be stabilized by collision with a third body so we do not need to consider the pre-reaction complex.[68] Thus the lowest energy at which tunneling can occur is the ground-state energy of separated reactants in the limit where the relative kinetic energy goes to zero, and this is used as the lower limit of the integral over energies when calculating the tunneling transmission coefficients in the MS-CVT/SCT calculations of $k_{TS,1}$, and $k_{TS,2}$. Rate constants calculated by eqs 12 and 13 with this lower limit on the tunneling energy will be called the low-pressure limit of the CCUS model (abbreviated LPL-CCUS).

4.2 High-Pressure-Limit CCUS Rate Constants

In the high-pressure limit, we again evaluate the rate constant by eqs 12 and 13. However, now the complex is assumed to be completely equilibrated by third-body collisions before the second dynamical bottleneck is crossed. Therefore tunneling can occur at all energies greater than or equal to the ground-state energy of the complex, which is lower than the ground-state energy or reactants, so the calculated rate constant is larger. Because we calculate the rate constants down to very low temperatures and down to the lowest energy state of the complex, the SCT tunneling calculations are carried out with the quantized-reactant-state tunneling (QRST) approximation, which is explained elsewhere.[69] Rate constants calculated by eqs 12 and 13 with this treatment of the tunneling energy will be called the high-pressure limit of the CCUS model (abbreviated HPL-CCUS).

In the pre-equilibrium model, the pre-reactive complex is formed, stabilized, and completely equilibrated. Thus the rate constants are given by eqs 2 and 3. Notice that if we neglect the TS,1 and TS,2 rate constants in the fractional prefactor of eq 12 and calculate the tunneling in the high-pressure limit, the result becomes equivalent to the PEM of eqs 2 and 3 because the properties of the complex cancel out in eqs 2 and 3 except for the ground-state energy of the complex providing the lower limit for the tunneling calculation. Thus, the PEM is computed as an approximation to the HPL-CCUS where we make the further assumption that the second bottleneck completely dominates the rate process.

4.3 MS-VTST/SCT

The MS-CVT/SCT method used to calculate the rate constants for passage through the second dynamical bottleneck in the above models is explained elsewhere,[19,22,24,68] and here we simply present a few details that will be useful for the discussion.

The first detail is to remind the reader that the effective barrier for tunneling is the ground-state vibrationally adiabatic potential curve given by[24,70]

$$V_a^G = V_{MEP}(s) + ZPE(s) \tag{14}$$

where $V_{MEP}(s)$ is the potential energy along the isoinertial minimum energy path (MEP), s is distance along the MEP, and $ZPE(s)$ is the zero point energy along the MEP.

The second detail is that we factorize the rate constants as follows:

$$k^{MS\text{-}CVT/SCT} = \kappa(T)\Gamma(T)k^{MS\text{-}TST}(T) \tag{15}$$

where κ is the SCT tunneling transmission coefficient, Γ is the CVT recrossing transmission coefficient, and

$$k^{MS\text{-}TST} = F_{act}^{MS\text{-}T}(T)k^{SS\text{-}TST}(T) \tag{16}$$

where $F_{act}^{MS\text{-}T}$ is the multi-structural torsional anharmonicity factor for TS,1 or TS,2 given by

$$F_{act}^{MS\text{-}T} = \frac{F^{MS\text{-}T,TSj}}{F^{MS\text{-}T,R}} \quad , \quad j = 1 \text{ or } 2 \tag{17}$$

and $k^{SS\text{-}TST}$ is the single-structure conventional transition state theory rate constant. Note that eq 15 writes the rate constant as a product of the multistructural conventional transition state rate constant $k^{MS\text{-}TST}(T)$ and an overall transmission coefficient that is itself factored into a tunneling transmission coefficient and a recrossing transmission coefficient. The multistructural conventional transition state rate constant is a quasiclassical one (which simply means that the reactive flux is calculated with classical reaction coordinate motion but other degrees of freedom quantized) computed with the transition state dividing surface passing through the saddle points of all conformations of the transition state. The recrossing transmission coefficient accounts for quasiclassical trajectories that recross the conventional transition state, and we estimate it using variational transition state theory to find the least recrossed transition state (within the flexibility allowed by our variational search, which is limited to dividing surfaces orthogonal to the minimum energy path). In MS-CVT/SCT, κ and Γ are computed using the minimum-energy path (i.e., the one through the lowest-energy conformer of the transition state); Γ measures the decrease in the rate constant when

one calculates the reactive flux at the maximum of the free energy of activation profile rather than at conventional transition state (which passes though the saddle point), and κ measures the increase in reaction rate due to quantum mechanical tunneling. Note that Γ is often called the variational effect.

5. RESULTS

5.1 Torsional anharmonicity factors

Figure 3a shows the multi-structural torsional anharmonicity factors $F^{\text{MS-T},\alpha}$ for methanol and the two transition structures. Figure 3b shows $F_{\text{act}}^{\text{MS-T}}$ for the CCUS model as calculated with eq 17. Note, the low-pressure limit and high-pressure limit of the CCUS model have the same $F_{\text{act}}^{\text{MS-T}}$ (as does the PEM). We can see in fig. 2 that the two pairs of mirror images of R1 are very close to each other in energy with a small energy gap of 0.83 kcal/mol, while there is a large energy difference (more than 7 kcal/mol) between the lowest-energy structures (the mutually mirror structures) and the two C_s symmetric structures of R2. Therefore, the factor $F^{\text{MS-T,TS2}}$ is smaller than $F^{\text{MS-T,TS1}}$ for $T > 300$ K; at temperatures lower than 300 K, the two factors are similar to each other. The reactant methanol has only one distinguishable structure, so for it, the torsional anharmonicity is only from torsion of methyl group. Figure 3b shows that the multi-structural torsional anharmonicity factors of the overall reactions are in the range 1.4–2.

5.2 Transmission Coefficients

Figure 4 shows the tunneling transmission coefficients κ^{SCT} as functions of temperature for both reaction R1 and R2 in both low-pressure and high-pressure limits. All of the tunneling transmission coefficients are approximately unity above 500 K, but they are huge at low temperature, for example, at 50 K, for the R2 reaction, the transmission coefficient is 2.7×10^4 and 1.1×10^{16} in the low-pressure limit and high-pressure limit, respectively. The larger tunneling effect in the high-pressure limit is because the stabilized pre-reactive complex is populated at low energies, and hydrogen can tunnel from more energy levels than in the low-pressure limit, where tunneling only occurs at energies above the ZPE of reactants.

Figure 4 also shows that the two reactions have almost the same tunneling transmission coefficients in the low-pressure limit. But in the high-pressure limit, the R2 reaction has an larger tunneling transmission coefficient than R1 at the same T, for example, at temperatures

lower than 200 K, we find that κ^{SCT} of reaction R2 is 1–3 orders of magnitude larger than that of R1. This is due to the wider barrier on the ground-state vibrationally adiabatic potential curve (V_a^G) of R1 than on that of R2, as shown in Figure 5.

Figure 6 shows the calculated recrossing transmission coefficients Γ as functions of temperature. Note that the recrossing transmission coefficients are independent of pressure. The figure shows variational effect is significant, especially for the low temperatures. Reaction R1 has a larger variational effect than R2. Remarkably large variational effects were also reported in previous work[17,68] for the hydrogen abstraction reactions of other alcohols by OH. This indicates that it is imperative to use variational transition state theory (rather than conventional transition state theory) to calculate the rate constants for this kind of reaction.

5.3 Preliminary Considerations About Rate Constants

First we consider the nonphysical rate constants that we have called $k_{TS,j}$; these are the rate constants computed for passage through TS1 or TS2 as if the first dynamical bottleneck (related to the association reaction) were not present. Note that the TS,j rate constants have the same transition states as the step b ones ($b1$ and $b2$), but the step b rate constants treat the complex as the reactant, whereas the TS,j rate constants treat the bimolecular reagents as the reactant. We use MS-CVT/SCT to calculate the TS,j rate constants in both the low-pressure limit and the high-pressure limit; these two limits of the MS-CVT/SCT rate constants differ only in the low-energy limit for tunneling, which is the zero-point level of separated OH + CH_3OH in the low-pressure limit, but is the zero-point level of OH$\cdots CH_3OH$ for the high-pressure limit.) As shown in Figure 7a, the MS-CVT/SCT reaction rate constants calculated using the SRP and generic scaling factors for frequency have gradually increasing differences as the temperature decreases, and the difference is up to a factor of 4 in the low-pressure limit, and up to ~3 orders of magnitudes in the high-pressure limit.

In Figure 8, we take the TS,1 treatment of reaction R1 in the low-pressure limit as an example to show in detail how the vibrational-frequency scaling factor affects the results. We can see that if the generic scaling factor is used, as opposed to the SRP scaling factor, the CVT rate constants will be underestimated significantly at ultra-low temperatures, while the tunneling will be overestimated. For example, at 50 K, the TS,1 MS-CVT rate constants in the low-pressure limit are 4.9×10^{-18} $cm^3\,molecule^{-1}\,s^{-1}$ and 8.4×10^{-20} $cm^3\,molecule^{-1}\,s^{-1}$ as obtained using respectively SRP and generic scaling factors, while the tunneling transmission coefficients are 3.5×10^4 and 5.6×10^5. The main reason for these large effects is that the

barriers including ZPE differ significantly when use the different scaling factors; the barrier on the effective potential for tunnelling is 1.36 kcal/mol with SRP and 1.76 kcal/mol with the generic scaling factor, respectively. (Note that these values do not match the 0 K results in Table 6 because Table 6 is for the conventional transition state, and the values quoted here are for the maximum of the ground-state vibrationally adiabatic barrier, which is more relevant for tunneling.) With the standard scaling factor, the vibrationally adiabatic barrier is higher, the MS-CVT rate constants are smaller, and the tunneling effect is larger.

Figure 7a shows the effect of neglecting the first dynamical bottleneck, which is equivalent in the high-pressure limit to using the pre-equilibrium approximation. The pre-equilibrium rate constants (HPL TS,j results) at ultra-low temperatures are unphysically high because the actual rate at low T is limited by the capture rate constant, which is ignored in this treatment.

Although the results in Figure 7a are nonphysical, we note that the MS-CVT/SCT reaction rate constants obtained using SRP scaling factor in the two limits both agree well with the experimental results at $T > 200$ K; at lower T, the experimental data are located between the calculated LPL and HPL TS,j results.

Now we include the presence of the first dynamical bottleneck by using the CCUS model. The phenomenological free energies of activation[71] of the two bottlenecks are listed in Table 7. These were obtained as follows:

$$\Delta G_{\text{act},a}^{\circ} = -k_{\text{B}}T \ln \frac{hC^{\circ}k_a}{k_{\text{B}}T} \tag{18}$$

and

$$\Delta G_{\text{act,TS,total}}^{\circ} = -k_{\text{B}}T \ln \frac{hC^{\circ}\left(k_{\text{TS,1}} + k_{\text{TS,2}}\right)}{k_{\text{B}}T} \tag{19}$$

where the latter is the free energy of the composite bottleneck obtained by joining the transition state dividing surfaces of the two products into a single dividing surface separating reactants from both products, and C° is the concentration (in molecules cc^{-1}) corresponding to the standard state of 1 bar. We can see that the composite bottleneck in the barrier region is always dominant in the low-pressure limit, while the bottleneck, TSa, to formation of the pre-reactive complex in the entrance region becomes dominant at low temperatures in the high-pressure limit. Thus it is necessary to consider both bottlenecks, and therefore our final rate constants are based on the CCUS model.

5.4 Final Calculated Rate Constants

The calculated rate constants in the low-pressure limit of the CCUS model (LPL-CCUS) and the high-pressure limit of the CCUS model (HPL-CCUS) are plotted as functions of temperature in Figure 7b, along with the experimental data and one set of calculated rates from the literature for comparison. The high-pressure-limit CCUS rate constants at low temperatures approach the capture rate constants. The final low-pressure-limit and high-pressure-limit CCUS rate constants (labeled with SRP) are in good agreement with the experiments and with those computed by Xu and Lin[8] for $T \geq 200$ K; at lower temperatures than 200 K, the experimental results are all between the HPL-CCUS and LPL-CCUS results, but much closer to those high-pressure-limit CCUS results.

The SRP calculations in Figure 7b (which are given in tabular form in Table S8 of the supporting information, along with the breakdown into the separate R1 and R2 rate constants) may be compared to three previous sets of calculations. Jodkowski et al.[9] calculated the rate constant in the low-pressure limit; their calculated rate constant increases from 7.6×10^{-13} (all rate constants in cm^3 molecule^{-1} s^{-1}) at 300 K to 4.4×10^{-11} at 1500 K, which is a factor of 1.2 larger than our low-pressure limit at 300 K, increasing to a factor of 2.8 larger at 1500 K. Galano et al.[10] calculated the rate constant in the high-pressure limit; their calculated rate constant increases from 6.8×10^{-13} at 298.15 K to 8.7×10^{-13} at 500 K, which is 18% lower than our high-pressure limit at 298.15 K and 44% lower at 500 K. The results of Xu and Lin are shown in the figure; they calculated the tunneling with the Eckart model in the high-pressure limit.

The final comparison is to the work of Siebrand and coworkers, including one of the present authors.[16] They included pressure effects using a kinetic Monte Carlo algorithm. Their results indicated that there is a very weak pressure effect due to the bath gas and that under the conditions of the experiment the calculated rate constants are far from the experimental observations and close to the low-pressure limit obtained in this work. Siebrand et al. pointed out that the presence of methanol dimers in a small amount may provide the required third body to partially stabilize the complex. Within that model, at 50 K the complex is stabilized by about 2 kcal/mol regarding to the energy of reactants and the calculated rate constants show a very good agreement with experiment.

The experiments at 82–88 K by both Martin et al.[13] and Shannon et al.[11] were performed at a pressure of ~0.4–1.2 torr. Our results indicate that at these pressures the pre-reactive complex should be formed because the experimental rate constants are much higher than the

LPL results obtained without considering its role. We conclude, to answer one of the questions in the introduction, that the experimental rate constants do include tunneling at energies below the energy of the bimolecular reactants. Our results also indicate that the complex is not completely stabilized under the experimental conditions because the high-pressure-limit CCUS model gives a higher rate than experiment. Hence, only intermediate degrees of stabilization of the pre-reactive complex can produce experimental rate constants between the two pressure limits. This is partly consistent with the conclusions[11,13] of Shannon et al., who, although they observed that the total rate constants were independent of pressure under their conditions, also concluded that the pre-reaction complex would be partially stabilized collisionally under the experimental conditions. They proposed that the reaction is dominated by the barrier of step b at room T but that "at very low temperatures ... the reaction is complete once the complex is formed," i.e., that the rate is dominated by the bottleneck of step a. However they also proposed that the reaction rate is determined by tunneling from partially stabilized energy levels of the complex at low T. They calculated a rate constant ($\sim 3 \times 10^{-12}$ cm^3 molecule^{-1}s^{-1}) at 82 K (see the Figure 2 in their paper) by using a master equation method. However, their results are about one order of magnitude smaller than their experimental values, which is the issue that led to Siebrand et al. to search for an alternative explanation to the experimental observations. It would be very interesting to recalculate the pressure-dependent rate constants at ultra-low temperatures.

Figure 7b shows that the rate constants calculated in the low-pressure limit of the CCUS model exhibit negative T dependence at low T. The high-pressure limit of the CCUS model shows negative temperature dependence only for 100 K $< T <$ 200 K, and the high-pressure-limit CCUS rate constants show a weak dependence on temperature for $T <$ 100 K; this is similar to the experimental observations.

5.5 Branching Fractions

Figure 9 plots the branching fractions of reactions R1 and R2 as functions of temperature in the high- and low-pressure limits of the CCUS model. The R1 reaction with its lower barrier height is dominant at higher temperatures, where this product constitutes up to 71% of the reaction. As the temperature decreases, the branching fraction to R2 increases, and the R2 reaction becomes dominant below 150 K at low pressure and at around 300 K at high pressure. In the high-pressure limit, the R2 branching fraction is close to 1 below $\sim$ 80 K. The predicted branching ratios in the high-pressure limit of the CCUS model are close to those obtained by Shannon et al.;[11] using a master equation, they predicted the turnover

temperature to be ~250 K at the experimental pressure. A previous theoretical study by Xu and Lin[8] did not predict a turnover; they predicted the branching ratio of R1 to be 96-89% over the whole 200-3000 K temperature range.

5.6 Temperature Dependence of KIEs

We also calculated the rate constants of the perdeuterated reaction $CD_3OD + OD$ using the CCUS model. As usual, the kinetic isotope effect is defined as the ratio of the light-species rate constant ($CH_3OH + OH$) to the heavy-species one ($CD_3OD + OD$). The calculated LPL-CCUS and HPL-CCUS KIEs are plotted as functions of temperature in Figure 10, where the rate constants are the sums of those for R1 and R2, i.e., the rate constants for loss of OH or OD. The tunneling effect is much larger for the undeuterated reaction than for the deuterated reaction, so the KIEs are larger than or close to unity at temperatures of interest in the present study. One sees the expected negative temperature dependence of the KIE in the low-pressure limit, but there is a nonmonotonic KIE variation with temperature in the high-pressure limit of the CCUS model. This is due to the competition of kinetic bottlenecks.

At ultracold temperatures $T < 70$ K the bottleneck for the formation of the entrance complex is rate determining and the KIE, η, is close to the unity

$$\eta = \frac{k^H}{k^D} = \frac{k_a^H}{k_a^D} \approx 1 \qquad (20)$$

because the rate constants of both the undeuterated and the deuterated reactions become equal to the capture rate constants, which are almost the same. At temperatures between 70 and 100 K the bottleneck for perdeuterated reaction starts to shift to the abstraction reaction (step b), whereas for the undeuterated compound is still the complex formation, and the KIE increases drastically. At temperatures above 100 K the bottleneck for reaction is the abstraction reaction for both the undeuterated and the deuterated compounds and so the KIEs are given by

$$\eta = \frac{k_{TS,1}^H + k_{TS,2}^H}{k_{TS,1}^D + k_{TS,2}^D} \qquad (21)$$

As temperature increases the HPL KIEs, although always larger than the LPL KIEs, because of the tunneling contribution in the former, become almost identical above 600 K.

6. SUMMARY

In this work, we calculated the forward rate constants of the reaction between methanol and OH over the temperature range 30-2000 K by employing the competitive canonical unified statistical (CCUS) model for both low-pressure and high-pressure limits, with the MS-CVT/SCT method to treat the barrier crossings. The CCSD(T)-F12a and CASPT2 methods were employed for validating various DFT model chemistries. Based on the validation studies, we selected M08-HX/jun-cc-pVTZ for potential energy surface direct dynamic calculations of reaction R1 and M08-SO/jun-cc-pVTZ for reaction R2. Similarly to what was found for other reactions of alcohols with OH, we found that the transition states had stronger anharmonicity of high-frequency vibrational modes than the reactants, so we used the specific-reaction-parametrized (SRP) scaling factors to take the anharmonicity of the zero-point energies and partition functions into account during the rate calculations.

We found that the negative temperature dependence of rate constants at low temperatures is caused mainly by the significant tunneling effect. At high temperatures, where there is no tunneling effect, the high-pressure-limit and low-pressure-limit results coincide with each other and agree well with the experimental results. At low temperatures, since the tunneling contribution depends on the degree of stabilization of the complex formed at various pressures, the rate constants become pressure-dependent. In the low-pressure limit, the stabilized complex cannot be formed collisionally, so the tunneling occurs at energies higher than the ZPE of the reactants; this leads to rate constants much lower than the experimental values measured at a low pressure. In the high-pressure limit, the complex is completely stabilized, and the energy range over which tunneling occurs is greatly extended; this leads to larger tunneling effects and strongly increased rate constants at low temperatures. When the reaction rate passing through the barrier region is comparable to the capture rate for the formation of the pre-reactive complex, the pre-equilibrium hypothesis will not hold, so that the pre-equilibrium model predicts unphysically high rate constants at ultracold temperatures.

In the CCUS model, which accounts for early and late dynamical bottlenecks, the high-pressure-limit rate constants for $T < 100$ K is dominated by the capture rate for the formation of the pre-reactive complex; the experimental data are found to be between the current high-pressure-limit and low-pressure-limit CCUS rate constants.

The anharmonicity of high-frequency modes of transition states is a very significant issue for calculating rate constants; this anharmonicity increases the rate constants at low temperatures by a factor of 4 to 11.

We also calculated the pressure-dependent branching fractions. In both the high-pressure and low-pressure limits, reaction R1 is dominant (with a branching fraction up to ~71%) at high temperatures due to the lower energy barrier as compared to R2. For $T < \sim 300$ K in the high-pressure limit and $T < \sim 150$ K in the low-pressure limit, reaction R2 becomes the dominant reaction because of its larger tunneling transmission coefficients and smaller variational effect.

We also studied the kinetic isotope effects, and we found that the calculated KIEs show a negative temperature dependence in the low-pressure limit and a dramatic nonmonotonic temperature dependence in the high-pressure limit due to the competition of early and late dynamical bottlenecks.

■ ASSOCIATED CONTENT

⑤ Supporting Information

The Supporting Information is available free of charge on the ACS Publications website at DOI:

Software and computational details, active spaces used in CASPT2 calculations for R2, calculated MUPDs of model chemistries, energy of the pre-reactive complex, rate constants and equilibrium constants of the capture reaction, $TS_{,j}$ MS-CVT/SCT rate constants, CCUS rate constants and KIEs, the M diagnostic, and the coordinates of optimized structures. (PDF)

■ AUTHOR INFORMATION

Corresponding Author
*E-mail: xuxuefei@tsinghua.edu.cn (XX), truhlar@umn.edu (DGT)

ORCID
Lu Gem Gao: 0000-0002-1666-0594
Jingjing Zheng: 0000-0003-3323-8157
Antonio Fernández-Ramos: 0000-0002-6468-1592
Donald G. Truhlar: 0000-0002-7742-7294
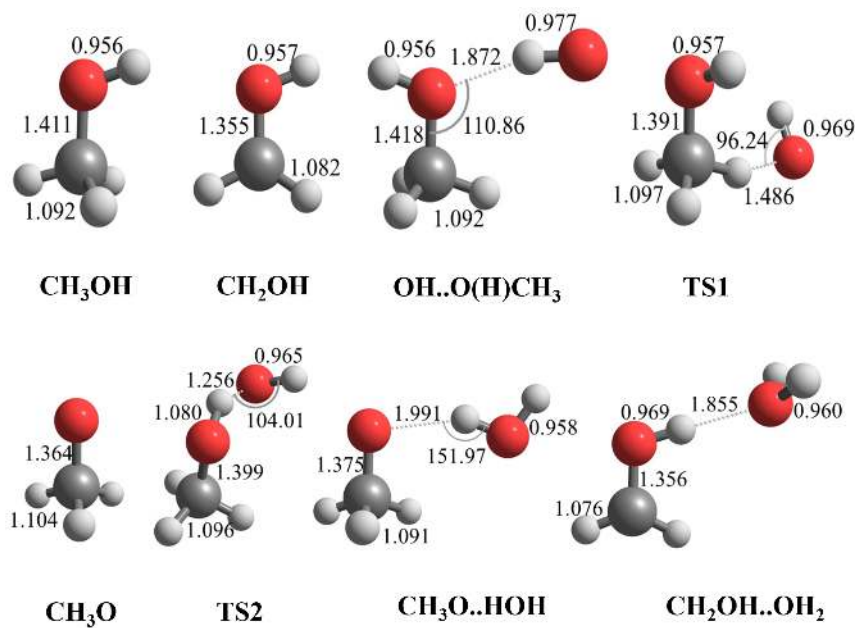Xuefei Xu: 0000-0002-2009-0483

Notes
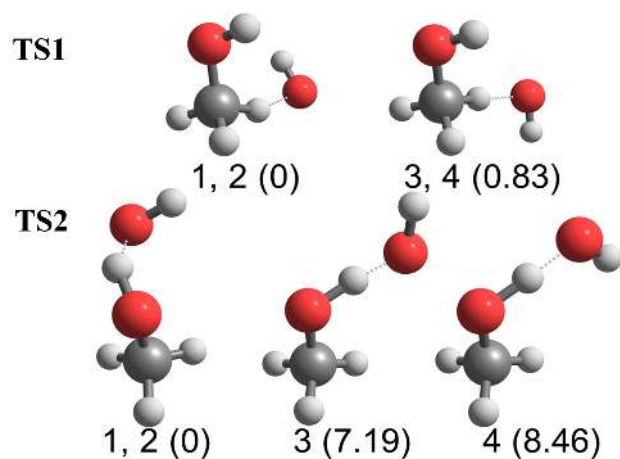The authors declare no competing financial interest.

■ ACKNOWLEDGMENTS

Fig. 1 Lowest-energy structures of all species and transition states obtained by M08-HX/MG3S. Bond distances are given in Å.

TS1

1, 2 (0)   3, 4 (0.83)

TS2

1, 2 (0)   3 (7.19)   4 (8.46)

Fig. 2 Conformers of transition states for reaction R1 (TS1) and R2 (TS2). Only one structure is shown for each pair of mirror images. The values in parentheses denote the relative energies (in kcal/mol) of the conformers with respective to the lowest-energy transition structure in each reaction. Energies for transition structures of reaction R1 are obtained by CCSD(T)-F12a/jun-cc-pVTZ//M08-HX/MG3S; energies for transition structures of reaction R2 are calculated by CASPT2(11,11)/MG3S//M08-HX/MG3S.

(a)

(b)
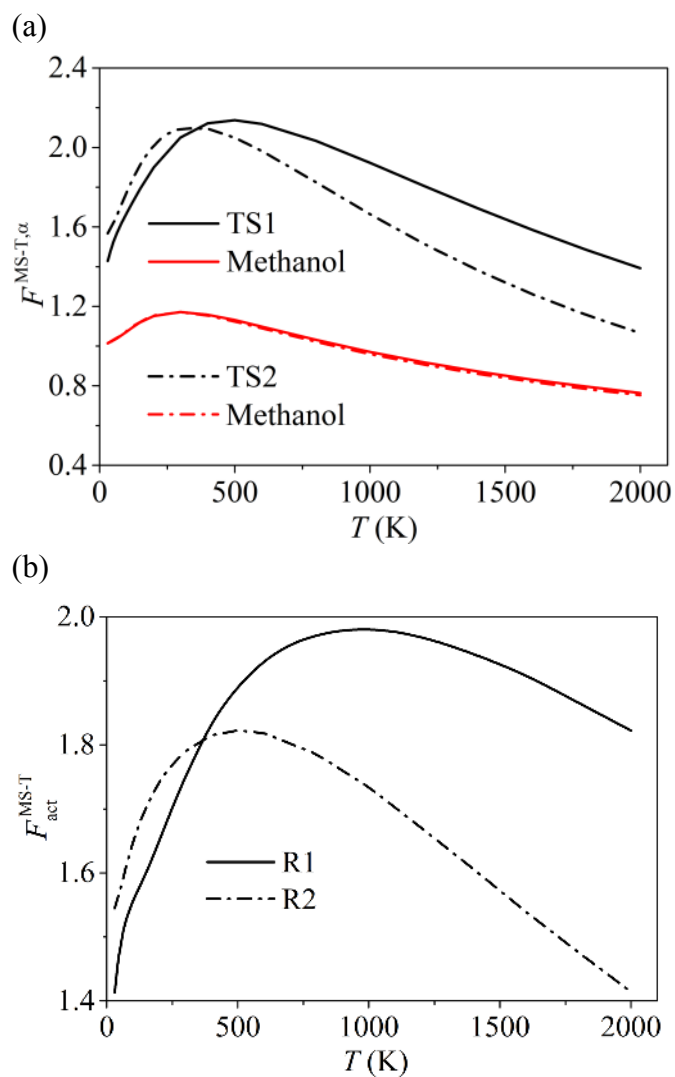
Fig. 3 (a) Multi-structural anharmonicity factors $F^{\text{MS-T},\alpha}$ for methanol and two transition states as computed for equilibrium structures and transition structures. Notice that the two methanol curves (which differ only because we use different electronic structure methods for R1 and R2) are almost identical. (b) Multi-structural anharmonicity factors $F^{\text{MS-T}}_{\text{act}}$ for reactions R1 and R2 in the CCUS model. Straight and dash–dot lines represent results for R1 by M08-HX/jun-cc-pVTZ and R2 by M08-SO/jun-cc-pVTZ.
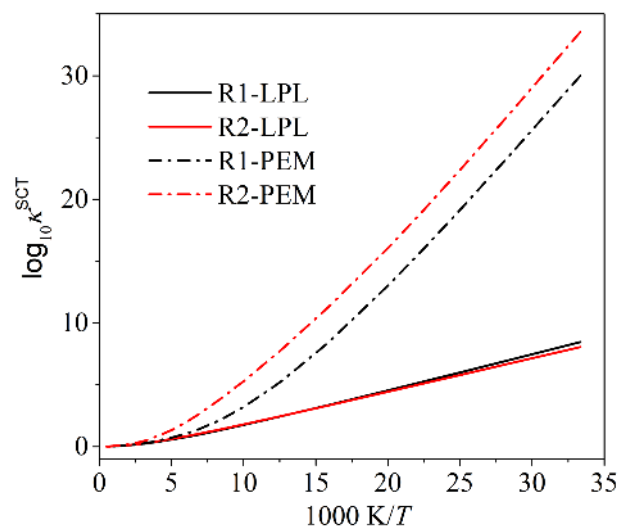
Fig. 4 Small-curvature tunneling transmission coefficients κ^{SCT} for reactions R1 and R2 in the low-pressure limit of the CCUS model (labeled as Rj-LPL) and in the high-pressure limit of the CCUS model and the pre-equilibrium model (labeled as Rj-PEM). The solid black line is hard to see because it is almost hidden under the solid red one.
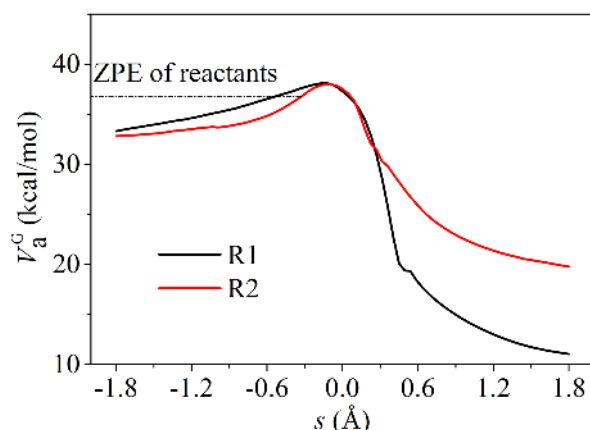
Fig. 5 Calculated ground-state vibrationally adiabatic potential curves (V_a^G) of reactions R1 and R2 as functions of the reaction coordinates s, where the reaction coordinates are scaled to a reduced mass of 1 amu. The zero of energy for this plot (and for all figures and tables in this paper) is the potential energy of the equilibrium geometry of the bimolecular reactants. In the low-pressure limit, the complex is not populated so there are no species with energy below the indicated zero point energy of bimolecular reactants (and therefore there is no tunneling below this energy). In the high-pressure limit, tunneling can occur at lower energies. For this figure (and for every place in the article where it is not explicitly stated otherwise), the calculations are based on the SRP vibrational scale factors.
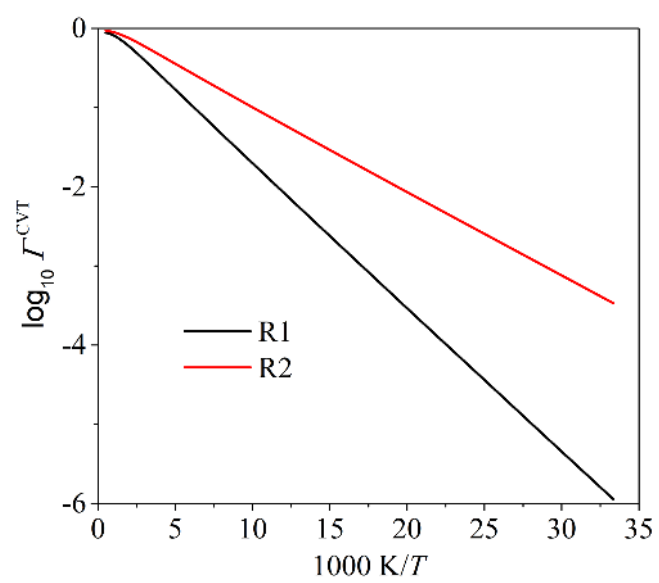
**Fig. 6** Recrossing transmission coefficients for reactions R1 and R2.

(a)

(b)
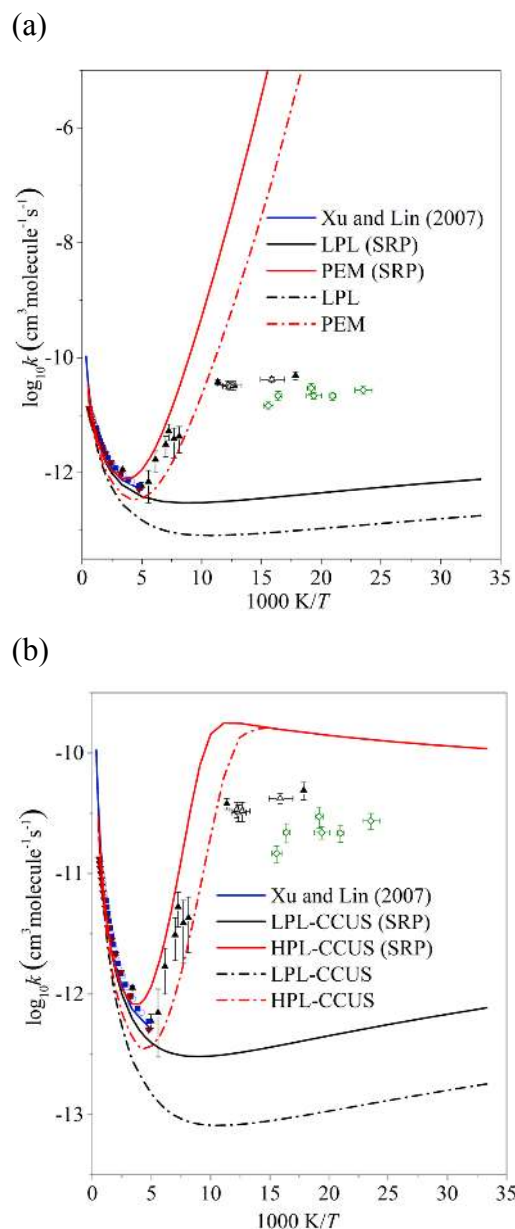
Fig. 7 Present theoretical results compared to one set of calculations from the literature and to experimental data; all results are total rate constants (sum of rate constants for R1 and R2). Previous theoretical results are from Xu and Lin.[8] Experimental data are from: (▲) Martin et al. (2014)[11]; (△) Shannon et al. (2013)[10]; (○) Atkinson et al. (1997)[72]; (■) Dillon et al. (2005)[7]; (◇) Antiñolo et al. (2016)[12]; (▼) Srinivasan et al. (2007)[73]. The present theoretical results are shown as dash–dot lines when obtained using the standard scaling factor for frequencies and as solid lines when obtained using SRP scaling factors and are as follows: (a) MS-CVT/SCT rate constant ($k_{TS,1}$ + $k_{TS,2}$) based on the tight transition state in the low-pressure limit (LPL) and in the high-pressure limit; the latter is the same as the total rate constant in the pre-equilibrium model and is labeled as PEM here. (b) Rate constants in the low-pressure-limit (LPL-CCUS) and the high-pressure-limit (HPL-CCUS) of the CCUS model.
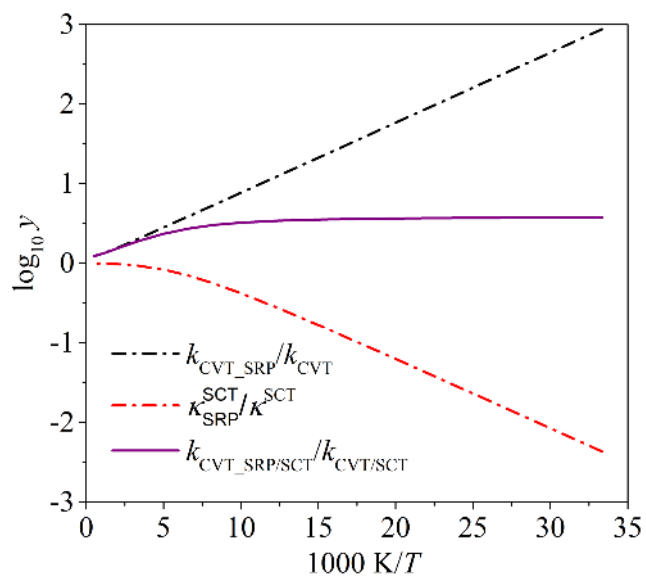
Fig. 8 Comparisons for reaction R1 of using the SRP scaling factor for frequencies vs. using the standard scaling factor for the MS-CVT approximation for the TS,1 rate constant. The subscript SRP denotes that the rate constant or tunneling transmission coefficient is obtained using the SRP scaling factor; while the others are obtained using the standard scaling factor; y is the ratio of results obtained using SRP and standard scaling factors.
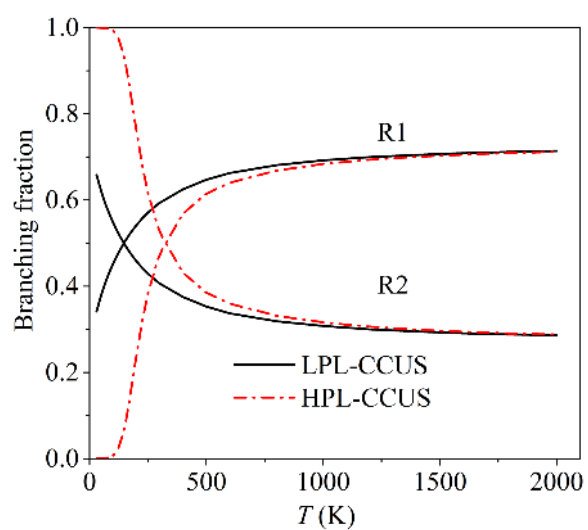
Fig. 9 Branching fractions of the OH + CH$_3$OH reactions calculated in the CCUS model. The dash–dot lines are for the high-pressure limit, and the solid lines are for the low-pressure limit.
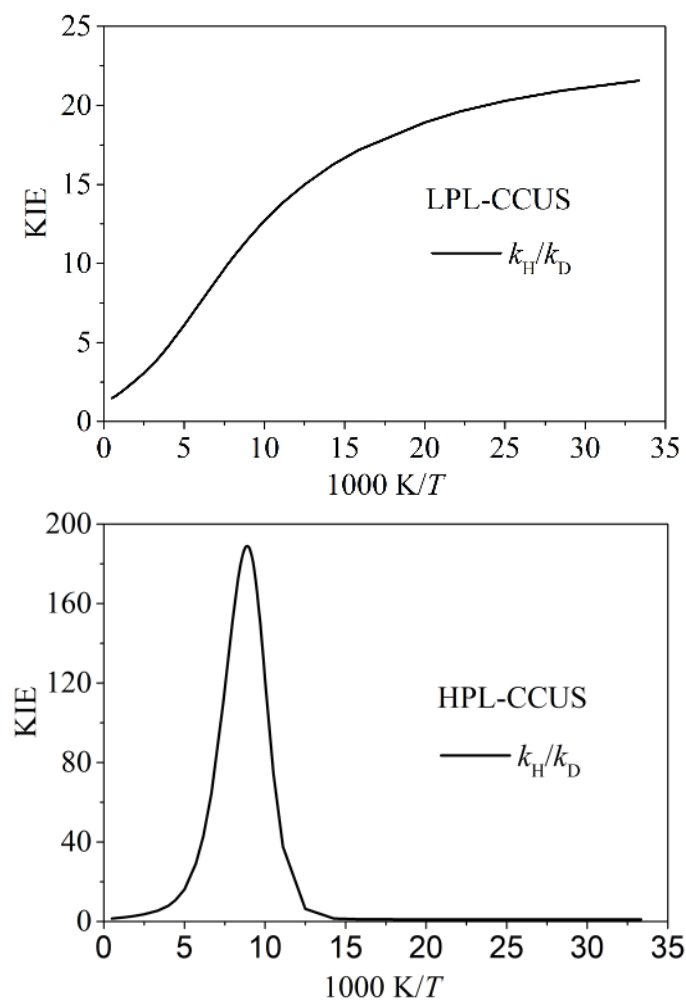
Fig. 10 Calculated KIEs in both low-pressure and high-pressure limits of the CCUS model.

Table 1. T_1 Diagnostic Values

OH	CH$_3$OH	CH$_2$OH...OH$_2$	TS1	CH$_3$O...HOH	TS2	H$_2$O	CH$_2$OH	CH$_3$O
0.008	0.010	0.015	0.028	0.018	0.055	0.009	0.018	0.024

Table 2. Experimental Enthalpies of Formation at 0 K and Zero-Point Energies (in kcal/mol) for Reactants and Products

species	CH$_3$OH	OH	CH$_2$OH	CH$_3$O	H$_2$O
$\Delta_f H_0^{o\,a}$	-45.44 ± 0.14	8.87 ± 0.07	-2.56 ± 0.17	6.79 ± 0.50	-57.10 ± 0.01
ZPE	31.85 ± 0.51[b]	5.29 ± 0.01[c]	22.59 ± 0.02[b]	22.60 ± 0.22[b]	13.26 ± 0.03[c]

[a]Xu and Lin[8]   [b]Meana-Pañeda et al[1e]   [c]Irikura et al.[46]

Table 3. Forward and Reverse Barrier Heights, Energies of Reaction, and Mean Unsigned Percentage Deviations from Best Estimates (in kcal/mol) for R1[a]

Method	$V_f^{\ddagger}$	$V_r^{\ddagger}$	ΔV	MUPD (%)
M06-2X/aug-cc-pVTZ	0.57	22.29	-21.72	22
M06-2X/jul-cc-pVTZ	0.60	22.28	-21.68	21
M08-SO/aug-cc-pVTZ	0.60	22.96	-22.36	21
M06-2X/jun-cc-pVTZ	0.63	22.31	-21.68	21
M06-2X/MG3S	0.68	22.12	-21.43	20
M08-SO/jul-cc-pVTZ	0.64	22.97	-22.33	20
M08-SO/jun-cc-pVTZ	0.68	23.02	-22.34	19
M05-2X/6-31+G(d,p)	0.88	21.31	-20.43	18
MPW1K/jul-cc-pVTZ	1.75	21.29	-19.55	13
MPW1K/jun-cc-pVTZ	1.74	21.31	-19.57	13
MPW1K/aug-cc-pVTZ	1.71	21.30	-19.58	12
MPW1K/MG3S	1.56	21.08	-19.52	9.1
M08-HX/MG3S	1.25	24.12	-22.87	7.4
M08-HX/aug-cc-pVTZ	1.38	24.37	-22.99	4.9
M08-HX/jul-cc-pVTZ	1.42	24.40	-22.97	4.0
M08-HX/jun-cc-pVTZ	1.48	24.47	-23.00	3.7
CCSD(T)-F12a/jun-cc-pVTZ[b]	1.46	23.34	-21.88	0.0
Exp.			-21.8± 0.6	

[a] All energies are relative to the energies of reactants (in kcal/mol) with ZPE excluded.

[b] Best estimate. The geometries are optimized at M08-HX/MG3S level.

Table 4. Forward and Reverse Barrier Heights, Energies of Reaction, and Mean Unsigned Percentage Deviations from Best Estimates (in kcal/mol) for R2[a]

Method	$V_f^{\ddagger}$	$V_r^{\ddagger}$	ΔV	MUPD (%)
MN15/jun-cc-pVTZ	1.27	14.87	-13.60	24
MPW1K/MG3S	4.66	17.73	-13.06	24
M05-2X/6-31+G(d,p)	1.47	14.42	-12.95	21
M08-HX/jun-cc-pVTZ	4.08	17.53	-13.45	18
M08-HX/jul-cc-pVTZ	4.05	17.47	-13.42	18
M08-HX/aug-cc-pVTZ	3.99	17.44	-13.45	17
M06-2X/MG3S	1.85	14.93	-13.08	16
M08-HX/MG3S	3.87	17.37	-13.49	16
M06-2X/jun-cc-pVTZ	1.94	14.90	-12.95	15
M08-SO/MG3S	2.15	15.57	-13.42	13
CCSD(T)-F12a/jun-cc-pVTZ[b]	3.98	16.30	-12.32	12
M08-SO/aug-cc-pVTZ	2.54	15.85	-13.30	8.6
M08-SO/jul-cc-pVTZ	2.58	15.86	-13.27	8.1
M08-SO/jun-cc-pVTZ	2.61	15.90	-13.29	8.0
CASPT2(11,11)/MG3S[b]	3.06	15.51	-12.45	0.0
Exp.			-12.4 ± 0.8	

[a] All energies are relative to the energies of reactants (in kcal/mol) with ZPE excluded.

[b] Best estimate. The geometries are optimized at M08-HX/MG3S level.

Table 5. Zero-Point Energies (in kcal/mol) and SRP Scaling Factors for TS1, TS2 and complex

	ZPE(Harm)[a]	ZPE(Anh)[a]	λ^{Anh}	λ^{H}	SRP λ^{ZPE}
TS1	38.25	37.38	0.977	0.986[b]	0.964
TS2	37.13	35.87	0.966	0.998[c]	0.964
Complex	40.50	39.80	0.983	0.986[b]	0.969
Complex	40.50	39.80	0.983	0.998[c]	0.980

[a] Calculated by MPW1K/MG3S.

[b] For M08-HX/jun-cc-pVTZ model chemistry

[c] For M08-SO/jun-cc-pVTZ model chemistry.

Table 6. Energetics (kcal/mol) for key stationary points[a]

Reaction[b]	Quantity[c]	Reactant	complex		Transition structure	
R1	ΔV	0.00	-6.53		1.48	
R2	ΔV	0.00	-6.55		2.61	
			standard λ	SRP	standard λ	SRP
R1	ΔH_0	0.00	-4.72	-4.91	0.93	0.54
R2	ΔH_0	0.00	-4.91	-5.04	1.50	0.78
R1	$\Delta H_{298.15}$	0.00	-5.17	-5.36	0.05	-0.32
R2	$\Delta H_{298.15}$	0.00	-5.25	-5.37	0.55	-0.14
R1	ΔH_{1000}	0.00	-3.47	-3.62	0.89	0.61
R2	ΔH_{1000}	0.00	-3.53	-3.63	1.23	0.71

[a] All values are for lowest-energy structure of the given species and are relative to reactants.
[b] Calculated by M08-HX/jun-cc-pVTZ for R1 and by M08-SO/jun-cc-pVTZ for R2
[c] ΔV is classical potential energy; ΔH_T is enthalpy at temperature T.

Table 7. Standard-state free energy of activation (in kcal/mol) for the association reaction and the total rate constant for barrier crossing

T(K)	$\Delta G^{\circ}_{\text{act},a}$	$\Delta G^{\circ}_{\text{act,TS,total}}$	
		HPL	LPL
30	0.19	-2.98	0.48
50	0.39	-1.65	0.96
100	0.99	0.80	2.27
150	1.66	2.82	3.63
200	2.39	4.56	5.00
298.15	3.92	7.48	7.69
400	5.60	10.27	10.35
600	9.13	15.57	15.60
1000	16.74	25.87	25.86
1400	24.84	35.96	35.93
2000	37.61	50.93	50.89

References:

[1] (a) Olah, G. A. *Angew. Chem., Int. Ed.* **2005**, 44, 2636. (b) Sarathy, S. M.; Oβwald, P.; Hansen, N.; Kohse-Höinghaus, K. *Prog. Energy Combust. Sci.* **2014**, *44*, 40. (c) Alecu, I. M.; Truhlar, D. G. *J. Phys. Chem. A* **2011**, *115*, 14599.(d)Li, S.; Tao, T.; Wang, J.; Yang, B.; Law, C. K.; Qi, F. *Proc.Combust.Inst.* **2017**, *36*, 709. (e) Meana-Pañeda, R.; Xu, X.; Ma, H.; Truhlar, D. G. *J. Phys. Chem. A* **2017**, *121*, 1693 and references therein.

[2] Jiménez, E.; Gilles, M. K.; Ravishankara, A. R. *J. Photochem. Photobio. A: Chem.* **2003**, *157*, 237.

[3] Hess, W. P.; Tully, F. P. *J. Phys. Chem.* **1989**, *93*, 1944.

[4] Wallington, T. J.; Kurylo, M. J. *Int. J. Chem. Kinet.* **1987**, *19,* 1015.

[5] Meier, U.; Grotheer, H. H. *Chem. Phys. Lett.* **1984**, *106*, 97.

[6] Bott, J. F.; Cohen, N. *Int. J. Chem. Kinet.* **1991**, *23*, 1075.

[7] Dillon, T. J.; Hölscher, D.; Sivakumaran, V.; Horowitz, A.; Crowley, J. N. Crowley. *Phys. Chem. Chem. Phys.* **2005**, *7*, 349.

[8] Xu, S.; Lin, M. C. *Proc.Combust.Inst.* **2007**, *31*, 159-166.

[9] Jodkowski, J. T.; Rayez, M.-T.; Rayez, J.-C.; Bérces, T.; Dóbé, S. *J. Phys. Chem. A* **1999**, *103*, 3750.

[10] Galano, A.; Alvarez-Idaboy, J. R.; Bravo-Pérez, G.; Ruiz-Santoyo, E. *Phys. Chem. Chem. Phys.* **2002**, *4,* 4648.

[11] Shannon, R. J.; Blitz, M. A.; Goddard, A.; Heard, D. E. *Nature Chem.* **2013**, *5*, 745.

[12] Hu, W.-P.; Truhlar, D. G. *J. Am. Chem. Soc.* **1996**, *118*, 860.

[13] Gomez Martin, J. C.; Caravan, R. L.; Blitz, M. A.; Heard, D. E.; Plane, J. M. *J. Phys. Chem. A* **2014**, *118*, 2693.

[14] Antiñolo, M.; Agúndez, M.; Jiménez, E.; Ballesteros, B.; Canosa, A.; Dib, G. E.; Albaladejo, J.; Cernicharo, J. *Astrophys. J.* **2016**, *823*, 25.

[15] Ye, L.L. Theoretical Investigations into Combustion Kinetics of Small Alcohol Systems, University of Science and Technology of China, Hefei, China (**2015**).

[16] Siebrand, W.; Smedarchina, Z.; Martínez-Núñez, E.; Fernández-Ramos, A. *Phys. Chem. Chem. Phys.* **2016**, *18*, 22712.

[17] Zheng, J.; Meana-Pañeda, R.; Truhlar, D. G. *J. Am. Chem. Soc.* **2014**, *136*, 5150.

[18] Zheng, J.; Oyedepo, G. A.; Truhlar, D. G. *J. Phys. Chem. A* **2015**, *119*, 12182.

[19] Yu, T.; Zheng, J.; Truhlar, D. G. *Chem. Sci.* **2011**, *2*, 2199.

[20] Zheng, J.; Yu, T.; Papajak, E.; Alecu, I. M.; Mielke, S. L.; Truhlar, D. G. *Phys. Chem. Chem. Phys.* **2011**, *13*, 10885.

[21] Zheng, J.; Mielke, S. L.; Clarkson, K. L.; Truhlar, D. G. *Comput. Phys. Commun.* **2012**, *183*, 1803.

[22] Zheng, J.; Truhlar, D. G. *J. Chem. Theory Comput.* **2013**, *9*, 1356.

[23] Zheng, J.; Meana-Paneda, R.; Truhlar, D. G. *Comput. Phys. Commun.* **2013**, *184*, 2032.

[24] (a) Lu, D.-h.; Truong, T. N.; Melissas, V. S.; Lynch, G. C.; Liu, Y. P.; Garrett, B. C.; Steckler, R.; Isaacson, A. D.; Rai, S. N.; Hancock, G. C.; Lauderdale, J. G.; Joseph, T.; Truhlar, D. G.

Comput. Phys. Commum. **1992**, *71*, 235. (b) Liu, Y. P.; Lynch, G. C.; Truong, T. N.; Lu, D. H.; Truhlar, D. G. *J. Am. Chem. Soc.* **1993,** *115*, 2408.

25 Garrett, B. C.; Truhlar, D. G. *J. Chem. Phys.* **1982**, *76*, 1853.

26 Hu, W.-P.; Truhlar, D. G. *J. Am. Chem. Soc.* **1995**, *117*, 10726.

27 Corchado, J. C.; Espinosa-Garcia, J.; Roberto-Neto, O.; Chuang, Y.-Y.; Truhlar, D. G. *J. Phys. Chem. A* **1998**, *102*, 4899.

28 Corchado, J. C.; Truhlar, D. G.; Espinosa-Garcia, J. *J. Chem. Phys.* **2000**, *112*, 9375.

29 Zhao, Y.; Truhlar, D. G. *J. Chem. Theory Comput.* **2008**, *4*, 1849.

30 Yu, H. S.; He, X.; Li, S. L.; Truhlar, D. G. *Chem. Sci.* **2016**, *7*, 5032.

31 Zhao, Y.; Truhlar, D. G. *Acc. Chem. Res.* **2008**, *41*, 157.

32 Yu, H. S.; He, X.; Truhlar, D. G. *J. Chem. Theory Comput.* **2016**, *12*, 1280.

33 Chai, J.-D.; Head-Gordon, M. *Phys. Chem. Chem. Phys.* **2008**, *10*, 6615.

34 (a) Becke, A. D. *Phys. Rev. A* **1988**, *38*, 3098; (b)Becke, A. D. *J. Chem. Phys.* **1993**, *98*, 5648; (c) Stephens, P. J.; Devlin, F. J.; Chabalowski, C. F.; Frisch, M. J. *J. Phys. Chem.* **1994**, *98*, 11623.

35 Lynch, B. J.; Fast, P. L.; Harris, M.; Truhlar, D. G. *J. Phys. Chem. A* **2000**, *104*, 4811.

36 (a) Dunning, T. H. *J. Chem. Phys.* **1989**, *90*, 1007 . (b) Kendall, R. A.; Dunning, T. H., Jr.; Harrison, R. J. *J. Chem. Phys.* **1992**, *96*, 6796.

37 Papajak, E.; Truhlar, D. G. *J. Chem. Theory Comput.* **2011**, *7*, 10.

38 Lynch, B. J.; Truhlar, D. G. *J. Phys. Chem. A* **2003**, *107*, 1384.

39 Hehre, W. J.; Radom, L.; Schleyer, P. v. R.; Pople, J. A. In *Ab Initio Molecular Orbital Theory* , Wiley: New York ,1986.

40 Rassolov V.; Pople, J. A.; Ratner, M.; Redfern, P. C.; Curtiss, L. A. *J. Comp. Chem.* **2001**, *22*, 976.

41 Raghavachari, K.; Trucks, G. W.; Pople, J. A.; Head-Gordon, M. *Chem. Phys. Lett.* **1989,** *157*, 479.

42 (a) Adler, T. B.; Knizia, G.; Werner, H.-J. *J. Chem. Phys.* **2007,** *127*, 221106. (b) Knizia, G.; Adler, T. B.; Werner, H.-J. *J. Chem. Phys.* **2009,** *130*, 054104.

43 Lee, T. J.; Taylor, P. R. *Int. J. Quant. Chem. Symp.* **1989**, *36, 199.*

44 Rienstra-Kiracofe, J. C.; Allen, W. D.; Schaefer, H. F. *J. Phys. Chem. A* **2000,** *104*, 9823.

45 Ruscic, B.; Boggs, J. E.; Burcat, A.; Csaszar, A. G.; Demaison, J.; Janoschek, R.; Martin, J. M. L.; Morton, M. L.; Rossi, M. J.; Stanton, J. F.; Szalay, P. G.; Westmoreland, P. R.; Zabel, F.; Berces, T.; *J. Phys. Chem. Ref. Data* **2005**, *34*, 573.

46 Irikura, K. K.; III, R. D. J.; Kacker, R. N.; Kessel, R. *J. Chem. Phys.* **2009,** *130,* 114102.

47 Xu, X.; Alecu, I. M.; Truhlar, D. G. *J. Chem. Theory Comput.* **2011***, 7*, 1667.

48 Tishchenko, O.; Zheng, J.; Truhlar, D. G. *J. Chem. Theory Comput.*, **2008**, 4, 1208.

49 Bao, J. L.; Sand, A.; Gagliardi, L.; Truhlar,D. G. *J. Chem. Theory Comput.* **2016**, *12*, 4274.

50 Zheng, J. Meana-Pañeda, R.; Truhlar, D. G. *Computer Phys. Commun.* **2013**, *184*, 2032.

51 Alecu, I. M.; Zheng, J.; Zhao, Y.; Truhlar, D. G. *J. Chem. Theory Comput.* **2010**, *6*, 2872.

52 Bloino, J.; Biczysko, M.; Barone, V. *J. Chem. Theory Comput.* **2012**, *8*, 1015.

53 Kuhler, K. M.; Truhlar, D. G.; Isaacson, A. D. *J. Chem. Phys.* **1996**, *104*, 4664.

55 Nielsen, H. H., The Vibration-rotation Energies of Molecules and their Spectra in the Infrared. In *Atoms III — Molecules I / Atome III — Moleküle I*, Flügge, S., Ed. Springer Berlin Heidelberg: Berlin, Heidelberg, 1959; pp 173-313.

56 Mills, I. M. Vibration-Rotation Structure in Asymmetric- and Symmetric-Top Molecules. In *Molecular Spectroscopy: Modern Research*; Rao, K. N., Mathews, C. W., Eds.; Academic: New York, 1972; pp 115-140.

57 Zhang, Q.; Day, P. N.; Truhlar, D. G. *J. Chem. Phys.* **1966,** *45*, 4948.

58 Bao, J. L.; Zheng, J.; Truhlar, D. G. *J. Am. Chem. Soc.* **2016**, *138*, 2690.

59 Tardy, D. C.; Rabinovitch, B. S. *J. Chem. Phys.* **1966,** *45*, 3720.

60 Penner, A. P.; Forst, W. *Chem. Phys.* **1975***, 11*, 243.

61 Troe, J. *J. Chem. Phys.* **1977,** *66*, 4745.

62 Baalbaki, Z.; Teitelbaum, H.; Dove, J. E.; Nip, W. S. *Chem. Phys.* **1986***, 104*, 107.

63 Barker, J. R.; Golden, D. M. *Chem. Rev.* **2003***, 103*, 4591.

64 Fernández-Ramos, A.; Miller, J.A.; Klippenstein, S. J.; Truhlar, D. G. *Chem. Rev.* **2006,** *106*, 4518.

65 Klippenstein, S. J.; Pande, V.; Truhlar, G. G. *J. Am. Chem. Soc.* **2014**, *136*, 528.

66 Truhlar, D. G.; Lu, D.-h.; Tucker, S. C.; Zhao, X. G.; Gonzàlez-Lafont, A.; Truong, T. N.; Maurice, D.; Liu, Y.-.P.; Lynch, G. C. *Am. Chem. Soc. Symp. Ser.* **1992***, 502*, 16.

67 Truhlar, D. G. *J. Chem. Soc. Faraday Trans.* **1994***, 90,* 1740.

68 Zheng, J.; Truhlar, D. G. *Faraday Discuss.* **2012,** *157*, 59.

69 Lauderdale, J. G.; Truhlar, D, G. *Surf. Sci.* **1985***, 164*, 558.

70 Truhlar, D. G.; Kuppermann, A. *J. Am. Chem. Soc.* **1971**, *93*, 1840.

71 Garcia-Viloca, M.; Gao, J.; Karplus, M.; Truhlar, D. G. *Science* **2004,** *303*, 186 .

72 Atkinson, R.; Baulch, D. L.; Cox, R. A.; Hampson, R. F.; Kerr, J. A.; Rossi, M. J.; Troe, J. *J. Phys. Chem. Ref. Data* **1997**, *26*, 521.

73 Srinivasan, N. K.; Su, M. C.; Michael, J. V. *J. Phys. Chem. A* **2007**, *111*, 3951.

TOC: